Nuclear Physics **A408** (1983) 525–558

PARTICLE PRODUCTION IN THE TARGET-RAPIDITY REGION FROM HADRON–NUCLEUS REACTIONS AT SEVERAL GeV

T.-A. SHIBATA*, K. NAKAI, H. EN'YO, S. SASAKI, M. SEKIMOTO and I. ARAI

Department of Physics, University of Tokyo, Hongo, Bunkyo-ku, Tokyo 113, Japan

and

K. NAKAYAMA, K. ICHIMARU, H. NAKAMURA-YOKOTA and R. CHIBA

Department of Physics, Tokyo Institute of Technology, Ohokayama, Megro-ku, Tokyo 152, Japan

Received 18 April 1983

Abstract: Highly inelastic processes in hadron-nucleus reactions at several GeV have been studied by measuring multi-particle emission in the target-rapidity region. Events with no leading particle(s) but with high multiplicities were observed up to 4 GeV. Proton spectra from such events were well reproduced with a single-moving-source model, which implied possible formation of a local source. The number of nucleons involved in the source was estimated to be $(3\text{–}5)A^{1/3}$ from the source velocity and the multiplicity of emitted protons. In those processes the incident energy flux seemed to be deposited totally or mostly (>75%) in the target nucleus to form the local source. The cross sections for the process were about 30% of the geometrical cross sections, with little dependence on incident energies up to 4 GeV and no dependence on projectiles (pions or protons). The E_0 parameter in the invariant-cross-section formula $E\,\mathrm{d}^3\sigma/\mathrm{d}p^3 = A\exp(-E/E_0)$ for protons from the source increases with incident energy from 1 to 4 GeV/c, but seems to saturate above 10 GeV at a value $E_0 = 60\text{–}70$ MeV. Three components in the emitted nucleon spectra were observed which would correspond to three stages of the reaction process: primary, pre-equilibrium and equilibrium.

E

NUCLEAR REACTIONS Cu (π^+, xp), (p, xp), p at 1.4, 2.5, 4 GeV/c; C, Pb (π^-, xp), (p, xp), p at 4 GeV/c; measured $\sigma(E_p, \theta)$, pp-coin. Cu (π^+, xn), (p, xn), p at 3 GeV/c, measured $\sigma(E_n, \theta)$. Al, Pb (π^-, X), (p, X), p at 2, 3, 4 GeV/c; C, Sn (π^-, X), (p, X), p at 4 GeV/c; measured changed particle multiplicity distribution, forward particle correlation.

1. Introduction

We have studied hadron–nucleus reactions in the energy range from 1 to 4 GeV, using beams from the KEK proton synchrotron [1,2]).

Recently, possible phenomena associated with nuclear matter at high baryon densities, or at high energy densities, have attracted experimental interest. A number of theoretical suggestions or speculations have been made for studies of the new phase of nuclear matter [3]). Being stimulated by those speculations, high-energy nucleus–nucleus collisions have been studied extensively in the past decade

* Present address, Max-Planck-Institut für Kernphysik, Heidelberg, Germany.

mainly at the Berkeley Bevalac, and great progress has been made in both experimental methods and theoretical concepts for understanding high-energy nuclear interactions [4]).

The progress at Bevalac was so fast, and the emphasis so much on the nucleus-nucleus collision, that heavy-ion reactions were studied in much more detail than hadron–nucleus reactions, leaving many fundamental questions. We do not know yet what would be the best energy for generation of the high densities: 200 MeV/nucleon, 2 GeV/nucleon or higher. To answer this question it is important to study the stopping power of the nuclear matter and mechanisms of energy deposition in nuclear matter [5]).

In the present work with hadron beams we studied:

(i) The stopping and energy deposition of GeV particles in target nuclei in order to pilot high-energy nucleus–nucleus experiments.

(ii) The space-time structure of nuclear excitations and decays in hadron–nucleus reactions, using the various experimental ideas and theoretical prescriptions developed in high-energy heavy-ion experiments [4]).

Through the interplay with high-energy heavy-ion experiments, with a common motivation to study new facets of nuclear matter, we were able to reach a more quantitative and detailed understanding of the stopping processes of GeV particles and the energy-deposition mechanisms in hadron–nucleus reactions.

In the following we shall report on the results of our first-phase experiment to investigate the features of the highly inelastic process following the bombardment of nuclei with GeV particles. We report on the determination of cross sections for highly inelastic processes, and propose a picture for the space–time evolution of the process. To study details of the energy deposition mechanisms, particularly the roles of formation of Δ's or other hadronic excited states, and possible multi-Δ correlations in the excited nuclear matter [6]), further experiments with a more sophisticated experimental system are in progress at this moment [7]).

2. Experimental procedure

Experiments were performed at the KEK $\pi 2$ channel which transported unseparated beams of pions and protons up to 4 GeV/c from an internal target at the 12 GeV proton synchrotron. A layout of the experimental setup is given in fig. 1. We measured inclusive proton spectra; two-proton coincidence and charged-particle multiplicity distributions with seven sets of ΔE-E telescopes and a cylindrical multiwire proportional chamber (CyMWPC) [8]). To obtain information on forward-emitted particles, nine blocks of plastic scintillator stacked in a 3×3 matrix configuration were used. A neutron detector was used to study the low-energy parts of the nucleon spectra. The dimensions of these detectors are listed in table 1. In the following subsections we describe each component.

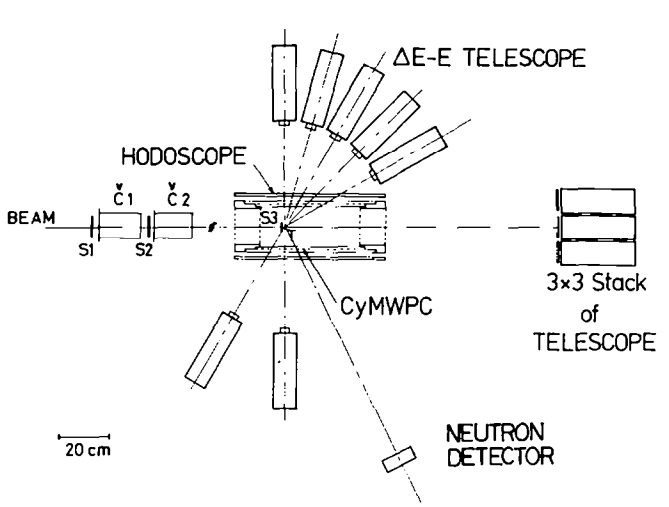

Fig. 1. Experimental layout.

TABLE 1

Summary of experimental conditions

(a) Compositions of positive beams from the $\pi 2$ beam line

Beam momentum (GeV/c)	Composition (%)		
	p	π^+	$e^+ + \mu^+$
1.4	53.4	37.5	9.2
2.5	63.4	28.6	8.0
4.0	77.6	15.6	6.8

(b) Dimensions of detectors

beam counters	
S1	$80 \times 80 \times 3$ mm^3
S2	$50 \times 50 \times 3$ mm^3
S3	$10 \times 10 \times 1$ mm^3
C1, C2	165 mm dia $\times$ 930 mm
$\Delta E - E$ telescopes	
ΔE1-ΔE7	$45 \times 45 \times 20$ mm^3 (in earlier runs) $45 \times 45 \times 7$ mm^3 (in later runs)
E1–E7	$100 \times 100 \times 300$ mm^3
CyMWPC	
sensitive layer	300 mm dia $\times$ 400 mm (220 wires)
hodoscope scintillators	
H1–H2	$500 \times 75 \times 5$ mm^3
forward counters	
ΔF1-ΔF9	$80 \times 80 \times 5$ mm^3
ΔF0	$45 \times 45 \times 7$ mm^3
F1–F9	$100 \times 100 \times 300$ mm^3
neutron counters	
N1	127 mm dia $\times$ 51 mm (NE213)
V1	$150 \times 150 \times 5$ mm^3

2.1. INCIDENT BEAMS AND TARGETS

Beams from the $\pi 2$ channel were defined and monitored by a threefold telescope of plastic scintillators (S1, S2, S3) and two sets of gas Čerenkov counters (C1, C2) placed downstream at the last dipole magnet of the $\pi 2$ channel. Beam signals were generated by

$$\text{"beam"} = \text{S1} \cdot \text{S2} \cdot \text{S3}\,,$$

and protons, pions and electrons(+muons) were identified as

$$\text{"p"} = \text{"beam"} \cdot \overline{\text{C1}} \cdot \overline{\text{C2}}\,, \qquad \text{"}\pi\text{"} = \text{"Beam"} \cdot \text{C1} \cdot \overline{\text{C2}}\,,$$

$$\text{"e}+\mu\text{"} = \text{"Beam"} \cdot \text{C1} \cdot \text{C2}\,.$$

The pressure of the Freon-12 $(CCl_2F_2)_n$ gas in C1 and C2 was tuned in a range from 0 to 4 atmospheres to satisfy the above conditions for each beam momentum. Efficiencies of the gas Čerenkov counters were checked to be better than 95% with 3 GeV/c negative beams, $\pi^- + \mu^- + e^-$. An example of the performance for positive beams is shown in fig. 2. For 1.4 GeV/c runs, particles were identified by measuring 15 m time-of-flight signals between a beam hodoscope at the intermediate focus point in the $\pi 2$ channel and a beam-defining counter near the target. Particle ratios at 1.4, 2.5 and 4.0 GeV/c are listed in table 1a.

The effective area of the targets was defined as $10 \times 10\,\text{mm}^2$ by the S3 counter placed in front of the target. Target thicknesses ranged from 1.0 to 2.0 g/cm^2 depending on the experiment. Beam intensities were typically 10^5 particles per

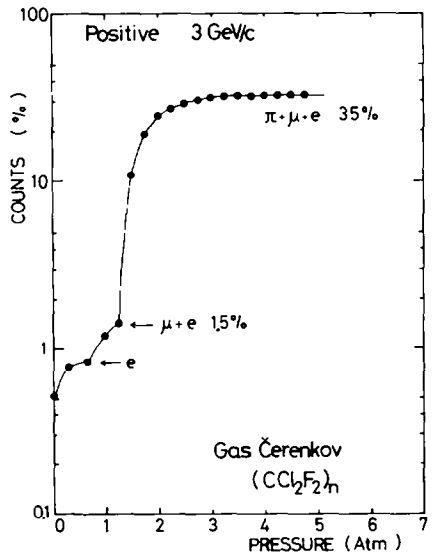

Fig. 2. An example of the data showing the performance of the gas Čerenkov counter.

pulse (of 0.3 sec width every 2.5 sec). The beam momentum was calibrated at 1, 2, 3 and 4 GeV/c by the time of flight of pions and protons using a path length of 8.7 m between S1 and another counter placed downstream. The accuracy of the beam-momentum calibration was within 0.3% while the momentum width of the beam was ±2%.

2.2. THE $\Delta E-E$ TELESCOPES

Seven sets of $\Delta E-E$ telescope were used to detect protons emitted in the target-rapidity region. They were set at 40 cm from the target and at $\theta_{lab}=30°$, 45°, 60°, 75°, 90°, −90° and −120°. The E-counters were made of NE110 plastic scintillators, 100×100 mm^2 in area and 300 mm long, and mounted on two-inch photomultipliers. ΔE counters made of plastic scintillators, of dimension $45\times45\times20$ mm^3, were used in the earlier experiments (at 1.4 GeV/c on the C target, and 4 GeV/c on the C and Cu targets); they were replaced by thinner ones, of dimension $45\times45\times7$ mm^3, for the later experiments (at 2.5 GeV/c on the Cu target, and 4 GeV/c on the Pb target).

Energy calibrations of the ΔE and E counters were made by time of flight in a separate run in each beam time. The protons emitted from a thick Cu target (30 mm) were used for the calibration. In the calibration run the seven ΔE-E telescopes were placed at a distance of 2 m from the target. Time-of-flight signals of protons between the target and ΔE counters and the pulse heights in the $\Delta E-E$ counters were recorded event by event. The start pulse was taken from the S1 counter which was replaced by a thicker one of 20 mm thickness in the calibration run. The time resolution of the time of flight was 500 psec, which corresponded to $\Delta E/E=5\%$ for 50 MeV protons and 8% for 150 MeV.

The possible gain drift of the E-counter photomultiplers was monitored by recording pulses induced by a LED (light-emission diode) mounted on the lucite light guide. The LED trigger mode was mixed in a usual trigger mode throughout the experiments with a rate of roughly one per twenty triggers.

2.3. NEUTRON DETECTOR

Since the low-energy parts of the proton spectra are generally distorted by the Coulomb effect as well as the energy loss in targets, neutrons were measured to study the low-energy nucleon spectra. By combining the neutron and proton spectra, the mechanism of nucleon emission from excited target nuclei was studied.

Neutrons were detected with a liquid-scintillation counter 127 mm in diameter and 51 mm in length. The liquid scintillator, NE213, was filled in a container in the form of a 1 mm thick aluminum cylinder viewed by a 5 inch photomultiplier (RCA 4522) through a Pyrex glass window.

The neutron counter was placed at 60° to the beam at a distance of 1 m from the target. For measurements of neutron spectra, a copper target as thick as 36 mm was used to improve the signal-to-noise ratio.

The neutron energy was measured from the time-of-flight between the target defining counter S3 and the liquid scintillator. The time resolution was 600 psec, corresponding to an energy resolution of 2% at 5 MeV and 4% at 20 MeV.

A plastic scintillation counter of $150 \times 150 \times 5$ mm^3 (V1) was placed in front of the liquid scintillator to veto charged particles. Gamma rays were eliminated by pulse-shape discrimination [9]. A correction for the neutron-detection efficiency was made using the data in ref. [10]).

2.4. CYLINDRICAL MWPC

To measure charged-particle multiplicity distributions, a cylindrical multiwire proportional chamber (CyMWPC) with charge division read-out was fabricated [8]). It was designed to meet the following demands: (i) large solid-angle coverage, (ii) capability for detection of high multiplicity, and (iii) wide dynamic range to detect various particles from the target nucleus.

The CyMWPC was installed with its axis parallel to the beam direction, and the target was located on the central axis so that the chamber covered polar angles from 25° to 135°. The CyMWPC consisted of a single layer of 220 stainless-steel resistive wires in a cylindrical shape 300 mm in diameter and 400 mm long. Each wire spacing was 3 mm, which corresponded to an azimuthal angular resolution of 1.5°. However, in order to save the number of electronic read-out modules, every two neighbouring wires were connected, and the actual resolution was $\Delta\phi = 3°$. The position along the cylinder axis was read by the charge-division method with a resolution of typically $\Delta z = 8$ mm. Pulses from both ends of each wire were amplified with a LeCroy TRA1000 current amplifier and then fed to charge-sensitive CAMAC ADC's (LeCroy 2249W). The magic gas mixture was used. In a chamber performance test, with the use of a β-ray source, the efficiency was measured to be 97%. In the actual runs, the efficiency was reduced to 85% because the chamber had to be operated at a low voltage to avoid ADC overflow of large pulses caused by heavy fragments and slow particles.

The CyMWPC was surrounded with a set of trigger hodoscopes made of twelve plastic scintillators of size $500 \times 70 \times 5$ mm^3, each of the twelve covering 30° in azimuthal angle. The coincidence of the CyMWPC with the hodoscope was effective in reducing background events and signals due to misfires of the chamber.

2.5. FORWARD COUNTER SYSTEM

The forward counter system was made of nine blocks of plastic scintillator stacked in a 3×3 matrix configuration. Each block was a telescope of two plastic scintillation

counters named ΔF and F. The F-counters were the same as the E-counter of the $\Delta E - E$ telescope and the ΔF counters were of $80 \times 80 \times 5$ mm^3. For the central block, which was hit by the beam particles, an additional defining counter of $45 \times 45 \times 7$ mm^3 was set behind the ΔF counter.

The counter system had no capability to measure energies nor to identify particles, but only to count particles emitted in an angular range of $\theta_{lab} \lesssim 10°$. This geometry was chosen to cover the full angular range of the leading-particle distribution which was sharply peaked within 10°.

2.6. EXPERIMENTAL SETUP AND DATA-TAKING

A summary of experimental conditions for each run is given in tables 1 and 2. Experimental data were taken with the following three different trigger modes:

(1) "telescope-trigger" = "beam" · (ΔE1 + ΔE2 + · · · + ΔE7),

(2) "hodoscope-trigger" = "beam" · (H1 + H2 + · · · + H12),

(3) "neutron-trigger" = "beam" · (N1) · ($\overline{\text{V1}}$),

where ΔE1 to ΔE7 are the ΔE counters of the telescopes, H1 to H12 are the hodoscopes surrounding the CyMWPC, and N1 is the neutron counter. In the "telescope-trigger" mode the targets were set with a tilt angle of 45° to the incident beam while in the "hodoscope-trigger" mode they were set perpendicular to the beam. In the "telescope-trigger" mode the two hodoscope scintillators in the telescope plane were removed.

TABLE 2

Summary of data-taking runs

Beam (GeV/c)	Target				
	C	Al	Cu	Sn	Pb
			(i) telescope-trigger mode		
1.4			○		
2.5			○ ●		
4.0	○		○		○ ●
target (g/cm^2)	1.38		1.08		1.14
			(ii) hodoscope-trigger mode		
2.0		○ ●			○ ●
3.0		○ ●			○ ●
4.0	○	○ ●	○	○	○ ●
target (g/cm^2)	1.38	0.81	0.90	1.46	2.27
			(iii) neutron-trigger mode		
3.0			○		
target (g/cm^2)			320		

○: Inclusive data.

●: Correlated data with the forward particles.

Data acquisition and on-line data analyses for monitoring purposes were done with a PDP-11/34 system. Signals from each detector were sent to the PDP-11/34 through the CAMAC modules and a CAMAC control system called CCS-11 by use of a general purpose data-acquisition program named KEK-X [11]).

With data sizes of 100–200 words/event, data-taking rates were 150–200 events per beam pulse for every 2.5 sec.

3. Data analyses and experimental results

We describe here the data analysis procedures and experimental results for each trigger mode.

3.1. ENERGY CALIBRATION OF THE $\Delta E-E$ TELESCOPES

For the energy calibration of each telescope the two-dimensional plot of pulse height (V) versus time of flight (T) was fitted with the following function:

$$V = a/(T-T_0)^2 + b/(T-T_0) + c\,, \tag{1}$$

where T_0 was the time origin, and a, b and c were free parameters of the expansion. The uncertainty in the calibration was mainly due to the time resolution. The overall uncertainty in the calibration increased with energy and was 8% at 170 MeV, the highest energy measured.

3.2. INCLUSIVE PROTON SPECTRA

Inclusive proton spectra in the range from 40 MeV to 180 MeV were measured with the seven $\Delta E-E$ telescopes at angles of 30°, 45°, 60°, 75°, 90°, −90°, −120°. Particles were identified in the $\Delta E-E$ plot. An example of the data for particle separations in the $\Delta E-E$ plane is shown in fig. 3. The proton spectra were obtained by integrating counts in every 10 MeV bin in the E-counter. Then the differential production cross section was deduced from the proton yield as follows:

$$Y(E \text{ to } E+\Delta E) = IRN_{\mathrm{T}} \frac{\mathrm{d}^2\sigma}{\mathrm{d}E\,\mathrm{d}\Omega} \Delta E\,, \tag{2}$$

where I is the number of incident beam particles per sec, R the fraction of protons in the incident beam particles, N_{T} the number of target nuclei per cm^2, ΔE the size of the energy bin, and $\Delta\Omega$ the solid-angle acceptance of the telescope. For background subtraction, proton yields in an empty-target run were subtracted from those in a target-in run. This correction amounted to about 20% of which 10% was due to nuclear reaction in the target-defining counter S3 and the remaining 10% was ascribed to accidental triggers by background particles.

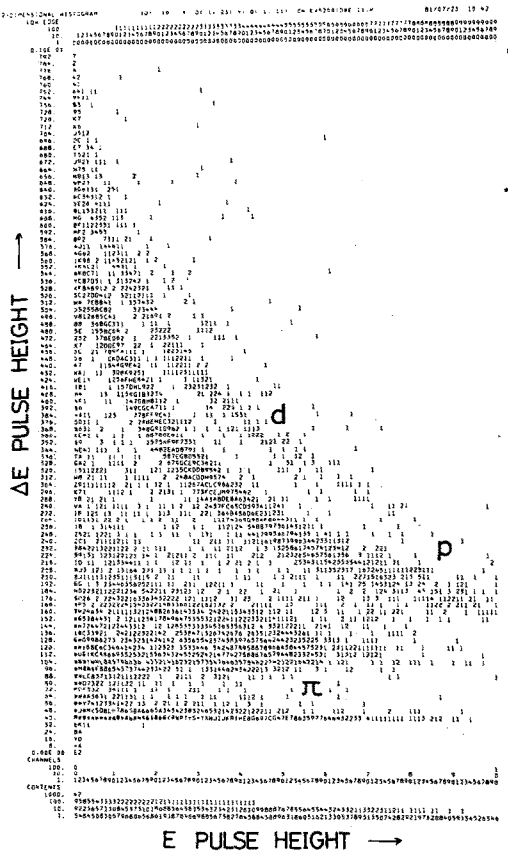

Fig. 3. An example of the $\Delta E - E$ plot for the identification of secondary particles.

Shown in table 3 and fig. 4 are invariant cross sections for proton production from the Cu target at 1.4, 2.5 and 4.0 GeV/c, and from the C and Pb targets at 4.0 GeV/c with both proton and pion beams.

3.3. PION YIELDS

Although we did not aim to measure pion yields in this experiment, pions were clearly separated from protons in the $\Delta E - E$ plot of the telescopes at large angles (90° and 120°), because the proton spectra did not tail toward high-energies. The inclusive cross sections, $d\sigma/d\Omega$, for pions are listed in table 4.

TABLE 3

Invariant doubly differential cross sections $E\,d^3\sigma/dp^3 = (1/p)\,d^2\sigma/dE\,d\Omega$ for proton production in units of b/sr · $(GeV/c)^2$c

Proton energy E_{lab} (MeV)	Angle θ_{lab}(deg)					
	30	45	60	75	90	120
			(a) $p(1.4\ GeV/c) + Cu \to p + X$			
60	2.66 (35)	1.42 (25)		1.69 (22)	0.83 (20)	0.36 (13)
70	2.49 (35)	1.14 (25)		1.34 (22)	1.19 (15)	0.61 (12)
80	2.27 (30)	2.43 (25)	1.23 (20)	0.79 (18)	0.60 (14)	0.24 (10)
90	1.85 (30)	1.26 (22)	1.50 (21)	0.90 (16)	0.44 (12)	0.17 (7)
100	1.99 (25)	1.11 (20)	0.89 (15)	0.67 (14)	0.37 (10)	0.148 (65)
110	1.46 (25)	0.97 (18)	0.59 (15)	0.70 (10)	0.22 (10)	0.080 (20)
120	0.66 (25)	0.79 (18)	0.37 (14)	0.34 (13)	0.12 (5)	0.034 (10)
130	0.98 (22)	0.61 (14)	0.35 (15)	0.43 (9)	0.08 (2)	
140	1.10 (20)	0.41 (14)	0.30 (14)	0.42 (9)	0.15 (4)	
150		0.45 (13)	0.24 (13)	0.18 (8)	0.15 (5)	
			(b) $p(2.5\ GeV/c) + Cu \to p + X$			
40	5.45 (35)	5.05 (30)	3.44 (35)	3.46 (30)	2.85 (14)	2.04 (20)
50	4.61 (35)	4.16 (25)	3.19 (30)	3.75 (30)	2.65 (15)	1.27 (15)
60	4.70 (12)	3.61 (25)	3.71 (30)	1.86 (25)	1.83 (13)	1.19 (16)
70	3.54 (25)	3.38 (25)	2.45 (25)	1.74 (20)	1.40 (9)	1.23 (13)
80	2.97 (22)	2.43 (18)	2.03 (20)	1.60 (18)	1.25 (10)	0.86 (13)
90	3.26 (25)	2.24 (18)	1.91 (25)	1.51 (18)	0.93 (8)	0.44 (7)
100	3.07 (20)	2.06 (20)	2.00 (20)	0.79 (14)	0.76 (10)	0.50 (8)
110	2.60 (20)	1.77 (18)	1.44 (15)	0.75 (10)	0.78 (7)	0.35 (7)
120	1.85 (13)	1.80 (15)	1.36 (15)	0.71 (12)	0.49 (6)	0.41 (7)
130	1.92 (16)	1.52 (14)	1.58 (18)	0.81 (9)	0.52 (6)	0.26 (6)
140	1.33 (13)	1.35 (15)	0.91 (18)		0.38 (6)	0.13 (4)
150					0.26 (5)	
			(c) $p(4.0\ GeV/c) + Cu \to p + X$			
60	4.02 (30)	2.51 (20)	2.62 (22)	1.70 (20)	1.12 (14)	0.95 (14)
70	3.94 (25)	2.75 (20)	1.72 (15)	1.66 (20)	1.19 (15)	0.95 (12)
80	3.35 (25)	2.94 (19)	1.71 (16)	1.23 (16)	1.22 (13)	0.59 (10)
90	3.00 (25)	2.51 (17)	1.48 (14)	1.15 (16)	0.85 (11)	0.57 (8)
100	1.95 (15)	2.27 (20)	1.25 (12)	0.96 (16)	0.71 (10)	0.40 (8)
110	2.20 (18)	1.18 (13)	1.18 (12)	0.85 (14)	0.64 (9)	0.39 (8)
120	2.07 (16)	1.30 (13)	0.70 (12)	0.75 (11)	0.52 (9)	0.27 (6)
130	1.83 (15)	1.54 (13)	0.87 (10)	0.88 (10)	0.44 (8)	0.26 (5)
140	1.60 (14)		0.73 (9)	0.59 (9)	0.38 (6)	0.17 (5)
150			0.60 (8)		0.30 (6)	
160					0.31 (6)	
			(d) $p(4.0\ GeV/c) + C \to p + X$			
60	0.786 (45)	0.404 (25)	0.186 (20)	0.330 (25)	0.212 (18)	0.108 (14)
70	0.720 (35)	0.487 (25)	0.292 (22)	0.322 (25)	0.208 (18)	0.104 (14)
80	0.721 (35)	0.469 (25)	0.322 (22)	0.318 (22)	0.176 (15)	0.046 (10)
90	0.673 (35)	0.403 (25)	0.259 (20)	0.266 (21)	0.150 (15)	0.040 (9)
100	0.391 (22)	0.419 (25)	0.212 (18)	0.209 (20)	0.104 (12)	0.040 (9)
110	0.473 (25)	0.230 (18)	0.191 (16)	0.250 (20)	0.094 (11)	0.030 (8)

TABLE 3 (CONTINUED)

Proton energy E_{lab} (MeV)	Angle θ_{lab}(deg)					
	30	45	60	75	90	120
120	0.389 (22)	0.256 (18)	0.188 (18)	0.177 (15)	0.074 (10)	0.019 (6)
130	0.370 (20)	0.255 (18)	0.165 (14)	0.145 (14)	0.061 (10)	0.029 (6)
140	0.327 (20)		0.133 (12)	0.113 (13)	0.052 (8)	0.019 (6)
150			0.125 (12)			
			(e) $p(4.0\ GeV/c)+Pb \rightarrow p+X$			
40	14.7 (5)	11.8 (5)	8.70 (55)	8.50 (55)	9.12 (45)	7.02 (35)
50	12.9 (5)	9.47 (40)	7.86 (50)	9.34 (45)	7.45 (30)	5.05 (30)
60	11.4 (4)	8.06 (45)	8.25 (55)	8.70 (40)	6.02 (30)	4.06 (25)
70	9.02 (40)	7.22 (40)	6.49 (40)	1.01 (40)	5.00 (25)	3.43 (20)
80	8.80 (35)	5.42 (30)	4.68 (35)	4.45 (25)	3.83 (25)	2.88 (20)
90	8.66 (40)	5.39 (25)	5.63 (45)	4.29 (25)	3.16 (18)	1.88 (15)
100	5.68 (30)	4.06 (30)	4.83 (30)	3.49 (25)	2.02 (20)	1.65 (14)
110	6.30 (30)	4.43 (25)	3.26 (25)	1.90 (18)	1.89 (12)	1.16 (12)
120	3.85 (20)	3.94 (22)	2.97 (25)	2.00 (20)	1.61 (18)	1.20 (15)
130	4.14 (25)	3.32 (20)	3.61 (30)	1.95 (16)	1.57 (14)	0.75 (12)
140	2.98 (25)	3.75 (22)	2.92 (30)	2.61 (20)	1.30 (11)	0.35 (7)
150					0.76 (10)	
			(f) $\pi(1.4\ GeV/c)+Cu \rightarrow p+X$			
60	3.53 (50)	1.78 (30)	2.04 (25)	1.45 (30)	1.35 (25)	0.61 (20)
70	3.06 (40)	1.90 (30)	1.42 (25)	1.94 (25)	1.99 (25)	0.90 (20)
80	2.84 (35)	1.47 (30)	1.08 (20)	1.32 (25)	1.19 (20)	1.21 (20)
90	1.84 (35)	1.21 (30)	0.79 (20)	1.22 (20)	0.83 (18)	0.49 (15)
100	2.34 (30)	1.03 (25)	0.55 (18)	0.76 (20)	0.46 (18)	0.53 (14)
110	1.80 (30)	1.02 (20)	0.38 (16)	0.72 (16)	0.30 (12)	0.52 (14)
120	0.97 (30)	0.86 (20)	0.48 (16)	0.72 (18)	0.53 (11)	0.24 (7)
130	1.73 (25)	0.82 (18)	0.69 (13)	0.52 (14)	0.17 (12)	
140	1.13 (20)	0.53 (15)		0.60 (12)	0.11 (7)	
150		0.58 (16)		0.47 (13)	0.27 (7)	
			(g) $\pi(2.5\ GeV/c)+Cu \rightarrow p+X$			
40	3.24 (40)	2.99 (40)	1.99 (40)	2.22 (35)	2.02 (25)	1.47 (25)
50	3.39 (45)	2.37 (30)	2.01 (40)	2.46 (30)	1.71 (30)	0.96 (22)
60	2.73 (35)	2.03 (30)	1.35 (40)	2.39 (30)	1.32 (22)	0.67 (22)
70	2.03 (30)	1.44 (30)	1.20 (25)	1.26 (25)	1.08 (20)	0.66 (18)
80	2.22 (30)	1.67 (25)	1.26 (25)	1.08 (20)	0.87 (18)	0.57 (18)
90	2.38 (30)	1.39 (22)	1.37 (30)	1.04 (20)	0.65 (16)	0.46 (11)
100	1.78 (25)	1.14 (20)	0.92 (25)	1.04 (18)	0.43 (12)	0.45 (11)
110	1.88 (25)	1.22 (22)	0.55 (20)	0.73 (12)	0.48 (13)	0.26 (9)
120	1.45 (15)	1.12 (18)	0.83 (18)	0.47 (14)	0.43 (9)	0.29 (11)
130	1.30 (18)	0.85 (13)	0.68 (22)	0.38 (11)	0.49 (13)	0.20 (10)
140	0.84 (18)	0.95 (18)		0.58 (13)	0.31 (10)	0.15 (6)
			(h) $\pi(4.0\ GeV/c)+Cu \rightarrow p+X$			
60	4.51 (80)	2.31 (45)	1.13 (30)	2.31 (50)	0.53 (25)	1.15 (30)
70	3.81 (55)	2.85 (45)	1.39 (35)	2.25 (35)	0.88 (45)	1.01 (25)
80	3.58 (55)	2.31 (40)	1.90 (40)	1.70 (35)	1.10 (30)	0.60 (22)

TABLE 3 (CONTINUED)

Proton energy E_{lab} (MeV)	Angle θ_{lab}(deg)					
	30	45	60	75	90	120
90	2.35 (60)	2.70 (40)	1.04 (30)	1.76 (35)	0.99 (25)	0.40 (22)
100	2.22 (35)	2.28 (45)	1.38 (35)	1.42 (35)	0.85 (25)	0.34 (18)
110	2.42 (35)	1.22 (30)	0.99 (25)	1.29 (30)	0.36 (15)	0.45 (15)
120	1.70 (35)	1.75 (30)	1.23 (30)	1.20 (30)	0.42 (14)	0.20 (18)
130	1.72 (35)	0.70 (25)	0.76 (20)	0.59 (20)	0.65 (20)	0.28 (13)
140	1.65 (30)		0.40 (20)	0.67 (18)	0.45 (15)	0.31 (13)
150			0.69 (18)			
			(*i*) $\pi(4.0\ GeV/c)+C\rightarrow p+X$			
60	0.79 (10)	0.37 (6)	0.15 (4)	0.271 (55)	0.11 (4)	0.20 (4)
70	0.676 (75)	0.339 (50)	0.288 (50)	0.280 (45)	0.155 (40)	0.13 (3)
80	0.524 (65)	0.302 (50)	0.242 (45)	0.190 (50)	0.154 (35)	0.089 (25)
90	0.618 (70)	0.372 (50)	0.184 (40)	0.184 (40)	0.095 (30)	0.045 (20)
100	0.380 (45)	0.273 (50)	0.127 (35)	0.222 (45)	0.074 (25)	0.012 (6)
110	0.422 (50)	0.187 (35)	0.145 (35)	0.129 (35)	0.074 (25)	0.052 (16)
120	0.309 (45)	0.326 (45)	0.190 (40)	0.138 (35)	0.076 (25)	0.02 (1)
130	0.304 (45)	0.165 (35)	0.174 (30)	0.134 (30)	0.078 (22)	0.037 (15)
140	0.292 (45)		0.130 (25)	0.152 (30)	0.063 (20)	0.035 (15)
150			0.123 (25)			
			(*j*) $\pi(4.0\ GeV/c)+Pb\rightarrow p+X$			
40	14.0 (1.5)	11.8 (1.2)	8.1 (9)	14.0 (1.2)		8.5 (1.0)
50	16.2 (1.5)	11.0 (1.0)	8.0 (9)	12.6 (1.2)	9.3 (1.0)	6.0 (8)
60	12.6 (1.2)	12.2 (1.2)	8.0 (9)	8.9 (1.0)	7.5 (9)	4.4 (9)
70	10.2 (1.0)	9.1 (1.0)	6.20 (70)	6.5 (8)	5.64 (60)	5.27 (55)
80	9.5 (9)	7.65 (65)	5.75 (50)	6.08 (70)	4.22 (60)	4.05 (55)
90	8.5 (1.1)	5.15 (60)	4.80 (70)	5.53 (75)	3.57 (55)	1.76 (35)
100	6.2 (9)	5.14 (50)	3.73 (50)	4.39 (60)	2.96 (40)	1.98 (35)
110	6.6 (8)	4.66 (60)	2.31 (40)	2.89 (35)	3.23 (50)	2.18 (35)
120	3.70 (55)	4.96 (55)	3.27 (45)	2.94 (50)	2.67 (35)	1.56 (40)
130	4.83 (55)	4.39 (55)	3.10 (40)	2.31 (40)	2.29 (50)	1.72 (30)
140	3.14 (50)	5.57 (55)	1.69 (50)	2.98 (20)	1.29 (30)	0.77 (15)

3.4. NEUTRON SPECTRA

Neutron spectra measured at 60° with 3 GeV/c protons and pions on Cu are shown in fig. 5. We were able to measure neutron spectra down to 3 MeV, which provided information complementary to the proton spectra. Invariant cross sections for neutron productions are listed in table 5.

3.5. CHARGED-PARTICLE MULTIPLICITY DISTRIBUTION

Charged-particle multiplicity distributions were measured using the hodoscope-trigger mode. The CyMWPC covered the polar region from 25° to 135°,

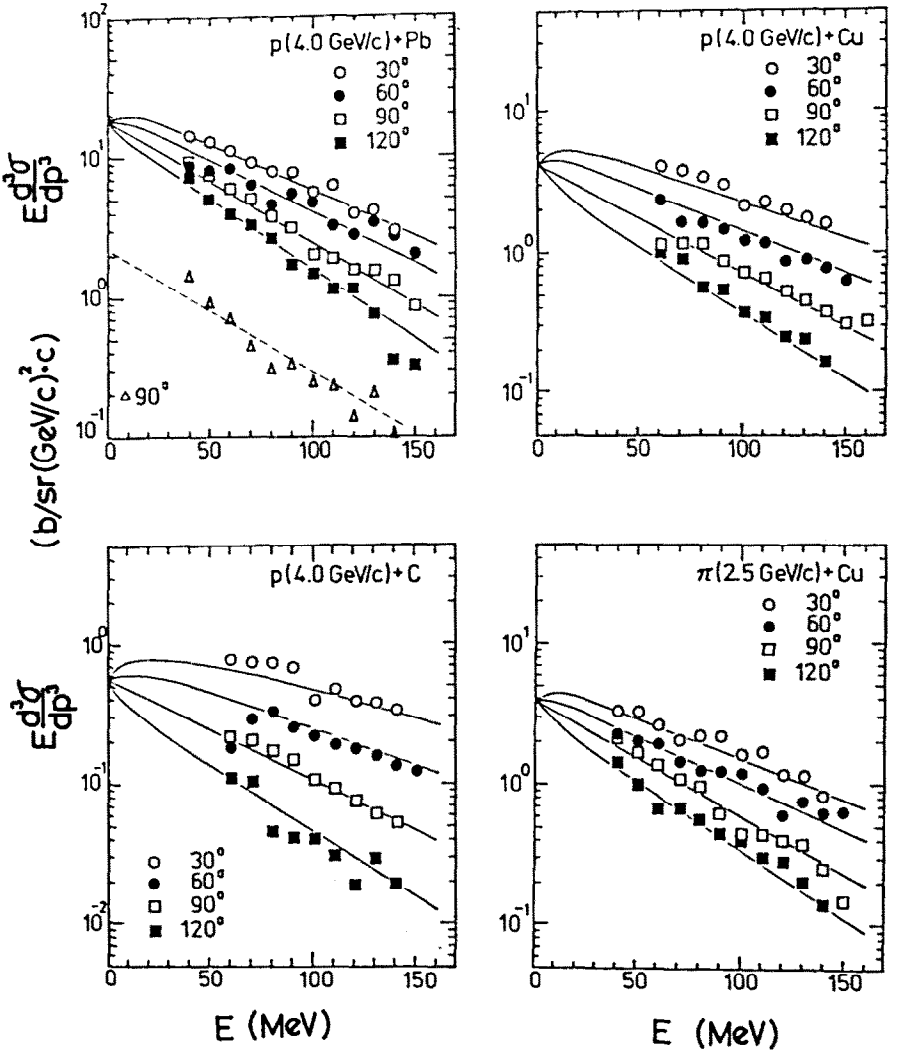

Fig. 4. Proton spectra, measured with the $\Delta E - E$ telescopes. Solid curves are best-fit curves using the single-moving-source model. Data points shown with triangles in the figure for p+Pb are 90° spectra taken with a trigger condition requiring at least one forward particle in $\theta_{lab} \leq 10°$.

TABLE 4

Charged pion production cross sections $(d\sigma/d\Omega)_+ + (d\sigma/d\Omega)_-$ at 90° and 120° from several GeV hadrons on nuclei (errors in pion cross sections are mainly due to those in particle identification)

Beam	p_{inc} (GeV/c)	Target	$(d\sigma/d\Omega)_+ + (d\sigma/d\Omega)_-$ (mb/sr)	
			90°	120°
p	1.4	Cu	2.9 (0.4)	1.4 (0.2)
π	1.4	Cu	17 (3)	11 (2)
p	2.5	Cu	20 (3)	12 (2)
π	2.5	Cu	25 (4)	16 (2)
p	4.0	Cu	30 (5)	20 (3)
π	4.0	Cu	40 (6)	26 (4)
p	13.0	Cu	74 (11)	
p	4.0	C	7.6 (1.1)	5.3 (0.9)
π	4.0	C	10 (2)	5.5 (0.8)
p	4.0	Pb	61 (9)	40 (6)
π	4.0	Pb	107 (16)	60 (9)

corresponding to 75% of the whole solid angle. For reduction of spurious tracks, each fire of the CyMWPC was required to coincide with the corresponding hodoscope.

The observed multiplicity distributions are shown in fig. 6a. Clearly, two components with high and low multiplicities are seen which seem to correspond to central and peripheral collisions, respectively. The distribution could be decomposed into a Poisson-type (high-multiplicity) and an exponential-type (low-multi-

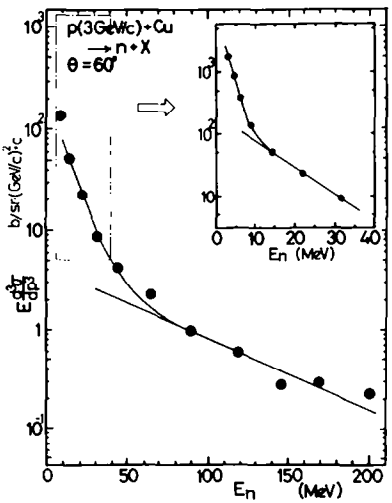

Fig. 5. Neutron spectrum at 60° from 3 GeV/c protons on a Cu target.

TABLE 5

Invariant cross sections $E\,d^3\sigma/dp^3 = (1/p)\,d^2\sigma/dE\,d\Omega$ for neutron productions at 60° from 3 GeV/c protons and pions on Cu in units of b/sr · $(\mathrm{GeV}/c)^2 c$

Neutron energy (MeV)	p + Cu	π^+ + Cu
3.3	1770 (30)	2580 (80)
4.5	900 (4)	1080 (60)
6.2	370 (10)	460 (30)
8.7	137 (4)	190 (13)
13.5	52 (2)	90 (6)
22	23 (1)	25 (2)
32	8.7 (0.4)	11 (2)
45	4.3 (0.3)	6.5 (0.9)
65	2.3 (0.1)	3.1 (0.3)
90	0.98 (0.07)	2.0 (0.3)
120	0.60 (0.04)	0.89 (0.14)
145	0.28 (0.04)	0.28 (0.11)
170	0.29 (0.03)	0.17 (0.03)
200	0.23 (0.03)	0.08 (0.03)

plicity) distribution. In order to understand these components, correlations with the forward particle(s) were studied.

3.6. CORRELATION WITH FORWARD COUNTER

The signal for the forward particles were defined as

$$\text{"forward tag"} = (\Delta\mathrm{F1}\cdot\mathrm{F1}) + (\Delta\mathrm{F2}\cdot\mathrm{F2}) + \cdots + (\Delta\mathrm{F9}\cdot\mathrm{F9}),$$

where (ΔF) was a TDC window and (F) was an ADC window.

Correlations between the rates of events with the forward particle(s) to all triggered events and the charged-particle multiplicities are plotted in fig. 7. The rates are strikingly small when the trigger condition requires high multiplicities ($M \geq 3$) in the CyMWPC, while they are large with low-multiplicity triggers ($M \leq 2$). Accordingly, when the charged-particle multiplicity distribution was taken with a trigger condition requiring no forward particle(s) the low-multiplicity part of the distribution was suppressed as shown in fig. 6b. The results indicate that in high-multiplicity events the incident particle or the leading particle(s) was stopped in the nucleus.

Events in the low-multiplicity component are considered to be due to peripheral processes. It should be noted, however, that part of the events could be due to accidental coincidences between background particles and beam particles. Although

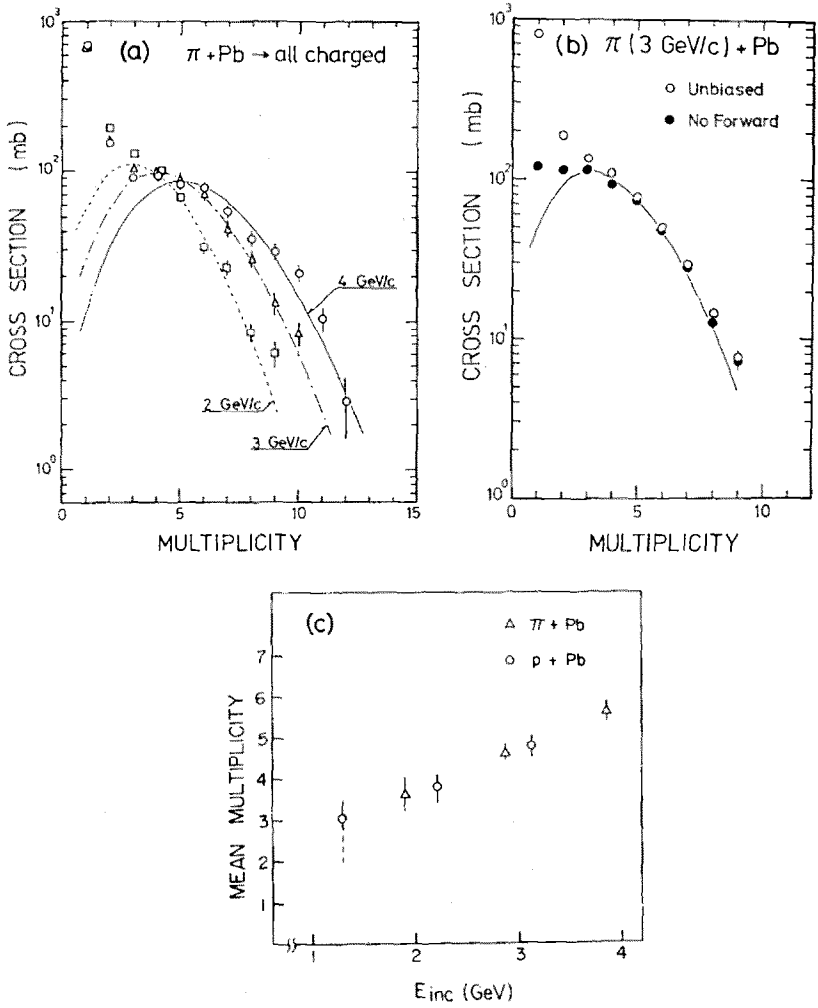

Fig. 6. Charged-particle multiplicity distributions observed by the CyMWPC which covered θ_{lab} = 25°–135° and ϕ = 0°–330°: (a) inclusive distributions; (b) comparison of a distribution with the trigger condition requiring no forward particle (●) with unbiased one (○); (c) mean multiplicities of the high-multiplicity components of the charged-particle multiplicity distributions measured by the CyMWPC.

the coincidence between the CyMWPC and a hodoscope scintillator at the corresponding position was made, it was hard to completely eliminate such a possibility with the single-layer MWPC. The high-multiplicity events are free from the accidental background. In this paper, therefore, we mainly discuss the high-multiplicity events and not the low-multiplicity events. Mean multiplicities of the high-multiplicity components (Poisson type) are plotted in fig. 6c versus total kinetic energies of projectile particles. The pion and proton incident data are in accord with each

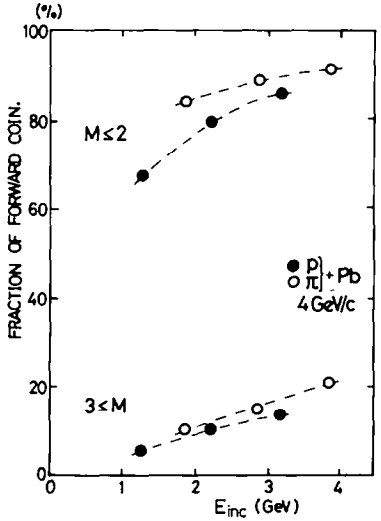

Fig. 7. Fraction of coincidence events with the forward-particle detector in all triggered events for low-multiplicity ($M \leq 2$) and high-multiplicity ($M \geq 3$) events in the target region. The low-multiplicity component may suffer possible contaimination due to accidental background events.

other when the total kinetic energy was used as a variable instead of the momentum. The independence of data on the type of projectile particle is a general feature of the present experimental data as seen in the following analyses and discussions. This fact suggests the stopping, or total energy deposition, of the projectile in the process studied.

3.7. SUPPLEMENTAL DATA WITH 12 GeV PROTONS OF NUCLEI

To supplement the present experimental results, data from a previous beam-survey experiment for the KEK $\pi\mu$ channel are used in the following discussions. In this experiment, the $\pi\mu$ channel was used as a particle spectrometer to measure particles emitted at 90° from nuclear targets bombarded by 12 GeV primary protons. Experimental details have previously been published elsewhere [12]), and the results have been partially reported. The composite particle production rates were used to deduce the size of interaction volumes via the coalescence model [13]).

Shown in table 6 and fig. 8 are inclusive cross sections for proton production at 90° with 12 GeV protons incident on C, Al, Ag and Ta targets. As discussed later the proton spectra clearly consist of two components. Although statistical errors were only ±3%, uncertainties in the absolute values due to the primary-proton intensity monitor and channel acceptance calculation have to be allowed for; these uncertainties were estimated to be 20% and 15%, respectively.

Inclusive cross sections for pion productions from C, Al and Cu targets are shown in table 6 and fig. 9. The statistical errors were ±3% and the systematic errors the

TABLE 6

Invariant cross sections $E\,d^3\sigma/dp^3 = (1/p)\,d^2\sigma/dE\,d\Omega$ for production of protons and pions at 90° from 12 GeV protons on nuclei in b/sr · $(GeV/c)^2 c$ (statistical errors are ±3%)

(a) Protons

Proton energy (MeV)	Target			
	Al	Cu	Ag	Ta
7.5	6.93	27.0	39.0	
12.0	4.03	14.0	22.0	41.0
17.0	2.80	9.2	14.8	25.3
23.0	2.07	6.6	10.7	16.5
30.0	1.58	5.0	8.0	12.3
38.0	1.25	3.9	6.2	9.3
47.0	1.00	3.1	4.8	7.3
56.0	0.81	2.5	3.8	5.8
66.0	0.66	2.0	3.1	4.7
90.0	0.44	1.35	2.0	3.2
115.0	0.28	0.87	1.3	2.1
140.0	0.20	0.61	1.0	1.5

(b) Pions

Pion energy (MeV)	Target					
	C		Al		Cu	
	π^+	π^-	π^+	π^-	π^+	π^-
45.0	387		740		1670	
88.0	235	223	445	402	990	1030
140.0	136	120	250	209	555	521
190.0	66.9	62.9	125	108	280	260
245.0	40.9	35.4	72.4	61.9	157	146
300.0	23.8	21.8	42.4	38.4	93.4	91.2
360.0	14.6	13.5	26.7	23.9	58.6	57.3
420.0	7.3	6.9	13.3	12.1	29.1	28.3

same as in the proton case. Composite particle spectra from the Al target are shown in fig. 10.

4. Discussions

4.1. THE HIGHLY INELASTIC PROCESS

When protons or pions at several GeV are incident on nuclei, we expect the following three major processes:

(a) nuclear elastic scattering,

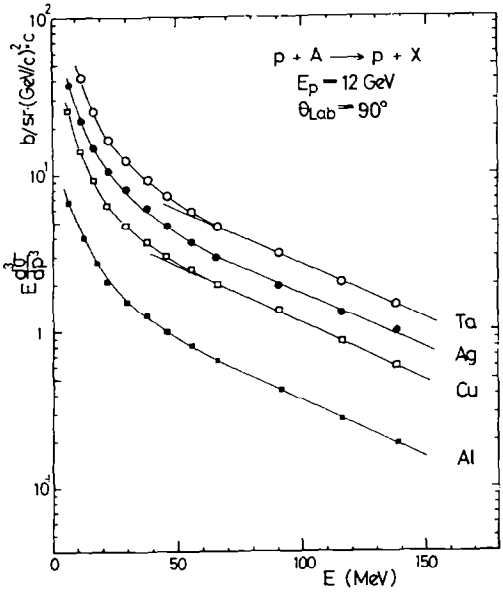

Fig. 8. Proton spectra at 90° from 12 GeV proton reactions on nuclei.

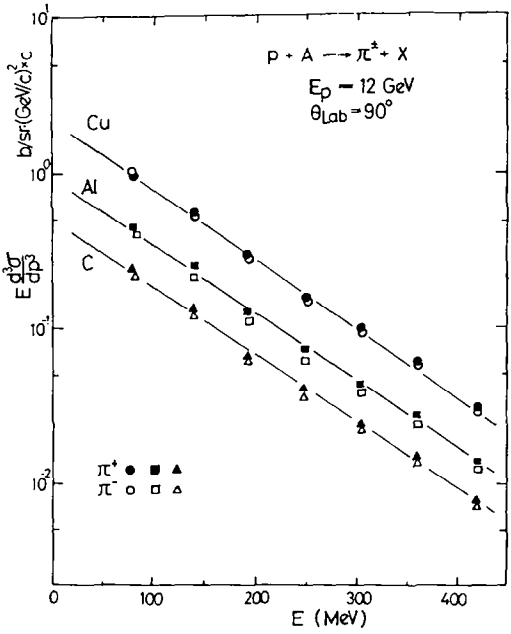

Fig. 9. Pion spectra at 90° from 12 GeV proton reactions on nuclei.

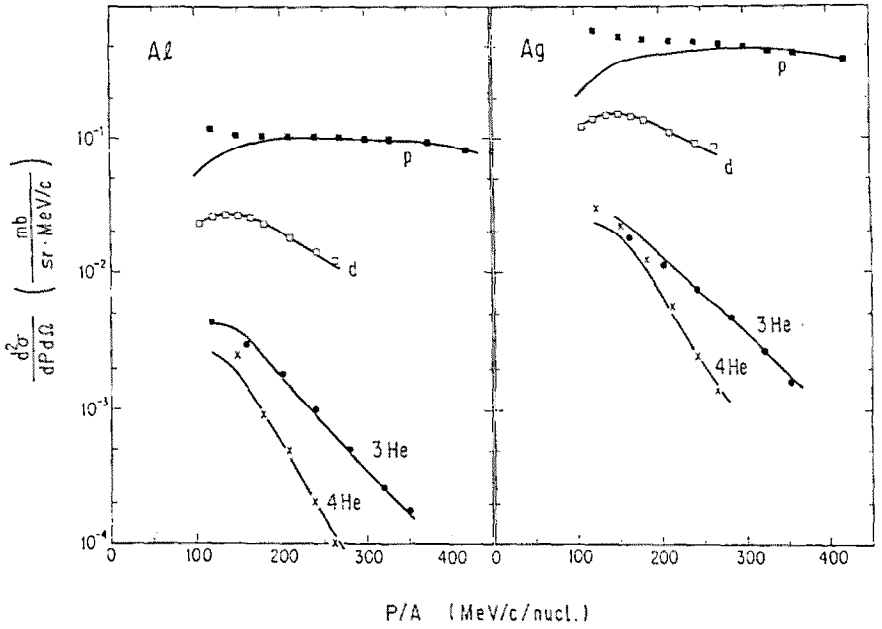

Fig. 10. Composite-particle spectra at 90° from Al and Ag targets bombarded by 12 GeV protons

(b) quasi-free nucleon-nucleon processes,

(c) highly inelastic nuclear processes.

The highly inelastic processes are characterized by multiple collisions of incident and secondary particles, and by deposition of a large fraction of the projectile energy in the target nucleus. The projectile would lose most of its energy, or stop in the nucleus.

The high-multiplicity events observed by the CyMWPC (fig. 6) must be due to the highly inelastic process. As described in subsect. 3.6, those events are characterized with no leading particle but with high multiplicity in the target-rapidity region. Cross sections for such events were deduced by fitting the multiplicity distributions with a Poisson-type plus an exponential-type distribution function and by integrating the Poisson components (see subsect. 4.4). Examples of cross sections deduced for different target nuclei are plotted in fig. 11. One can see that the cross sections are about 30% of the geometrical ones (calculated with $r_0 = 1.2$ fm).

We defined the cross section as the "stopping" cross section [1]) with quotation marks because in these highly inelastic processes the incident energy flow was totally (or mostly) stopped in a target nucleus. In the following sections, we shall discuss this in more detail in order to test the validity of this definition of "stopping".

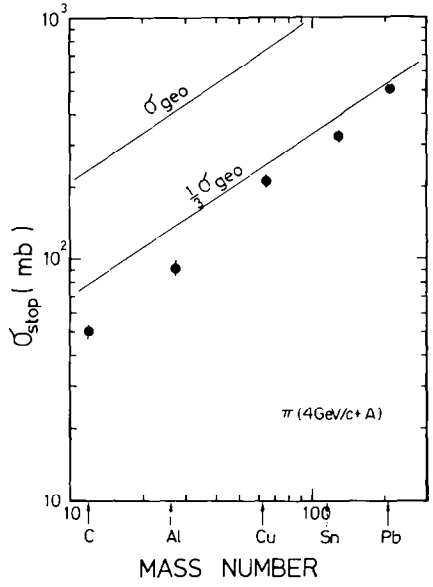

Fig. 11. The "stopping" cross sections versus target nuclear mass numbers. The geometrical cross sections were calculated with $r_0 = 1.2$ fm.

4.2. INCLUSIVE PROTON SPECTRA

The measured protons with kinetic energies from 40 to 170 MeV and at angles from 30° to 120° belong to a rapidity region $-0.3 < y < 0.6$, the target-rapditiy region. The spectra would, therefore, reflect excitation and decay mechanisms of target nuclei.

The inclusive proton spectra shown in fig. 4 were analyzed using a moving-source model [14]). In this model protons were assumed to be emitted isotropically from a single moving source with an exponential form,

$$E\frac{\mathrm{d}^3\sigma}{\mathrm{d}p^3} = A\,\exp\left(-E^*_{\mathrm{kin}}/E_0\right), \tag{3}$$

in a frame moving with velocity β_s relative to the laboratory frame. The asterisk indicates variables in the moving frame. The Lorenz transformation to the laboratory frame gives

$$E^*_{\mathrm{kin}} + m = (E_{\mathrm{kin}} + m - \beta_s p\,\cos\theta)/\sqrt{1-\beta_s^2}\,, \tag{4}$$

where θ is the angle of the detector in the laboratory frame. With this relation, eq. (3) is transformed as

$$E\frac{\mathrm{d}^3\sigma}{\mathrm{d}p^3} = A\,\exp\left(-\left(\frac{E_{\mathrm{kin}} + m - \beta_s p\,\cos\theta}{\sqrt{1-\beta_s^2}} - m\right)\Big/E_0\right). \tag{5}$$

TABLE 7

Summary of the moving source analyses

Beam	p_{inc} (GeV/c)	E_{inc} (GeV)	Target	A [a] b/sr · (GeV/c)^2c	β_s [a]	E_0 [a] (MeV)	$\sigma_{h.i.}$ [b] (b)	$\langle m_p \rangle$ [c]	$\langle n \rangle$ [d]	$\langle E \rangle$ [e] (GeV)	$\langle E \rangle \langle n \rangle$ (GeV)
p	1.4	0.73	Cu	4.69 (14)	0.162 (4)	44.8 (7)	0.25 (6)	2.7 (7)	5.9	0.083	0.49
π	1.4	1.25	Cu	5.32 (15)	0.116 (2)	51.7 (9)	0.37 (10)	2.6 (7)	5.6	0.087	0.49
p	2.5	1.73	Cu	6.14 (5)	0.139 (3)	57.7 (4)	0.36 (6)	3.7 (6)	8.0	0.098	0.79
π	2.5	2.36	Cu	4.52 (10)	0.134 (6)	54.2 (8)	0.18 (4)	5.5 (1.3)	12.0	0.093	1.11
p	4.0	3.17	Cu	5.45 (7)	0.171 (3)	57.6 (6)	0.24 (5)	4.8 (1.0)	10.5	0.103	1.08
π	4.0	3.86	Cu	4.90 (15)	0.190 (9)	58.3 (1.3)	0.19 (8)	7.6 (3.2)	16.5	0.107	1.77
p	4.0	3.17	C	0.829 (8)	0.229 (2)	62.3 (5)	0.085 (25)	2.3 (7)	4.7	0.121	0.57
π	4.0	3.86	C	0.632 (16)	0.243 (20)	68.0 (1.5)	0.10 (7)	1.8 (1.4)	3.5	0.131	0.46
p	4.0	3.17	Pb	*21.1 (1)*	*0.105 (1)*	*50.7 (2)*	*0.54 (4)*	*6.8 (5)*	17.2	0.084	1.44
π	4.0	3.86	Pb	20.0 (3)	0.094 (1)	57.7 (6)	0.44 (5)	9.6 (6)	24.2	0.093	2.25

[a]) $A \exp(-E/E_0)$ in the frame moving with β_s.

[b]) $\sigma_{h.i.}$: cross section for the highly inelastic process.

[c]) $\langle m_p \rangle$: mean multiplicity of protons.

[d]) $\langle n \rangle$: mean multiplicity of nucleons.

[e]) $\langle E \rangle$: average energy of nucleons.

The parameters involved in this formula are slope parameter E_0, the velocity β_s, and the normalization factor A.

The solid curves in fig. 4 were obtained by fitting eq. (5) to the experimental data. For ten different combinations of projetiles (pions or protons, with different energies) and targets (C, Cu or Pb), the proton spectra were reproduced with this simple model. The best-fit parameters, E_0, β_s and A, are listed in table 7. This result led us to a picture in which a moving source, or possibly a fireball-like object, was formed in the target-rapidity region and decayed by emitting protons.

In this analysis, the E_0 parameters were determined essentially by the proton spectra at $\theta = 90°$ while the degree of fan-out of spectra at different angles determined the parameter β_s.

When β_s is small ($\beta_s < 0.3$) eq. (5) approximates to

$$E\frac{d^3\sigma}{dp^3} = A \exp\left(-(E_{kin} - \beta_s p \cos\theta)/E_0\right), \tag{6}$$

and at $\theta = 90°$

$$E\frac{d^3\sigma}{dp^3} = A \exp\left(-E_{kin}/E_0\right). \tag{7}$$

Hence, the E_0 parameter can be determined by the 90° spectra as long as β_s is small. We determined the E_0 parameter at 12 GeV from the proton spectra in fig. 8 in the energy region from 60 to 140 MeV. The slope parameters E_0 versus incident particle energies are shown in fig. 12. The data at 0.24, 30 and 400 GeV were taken from refs. [15-17]), respectively. The E_0 parameter can be related to the

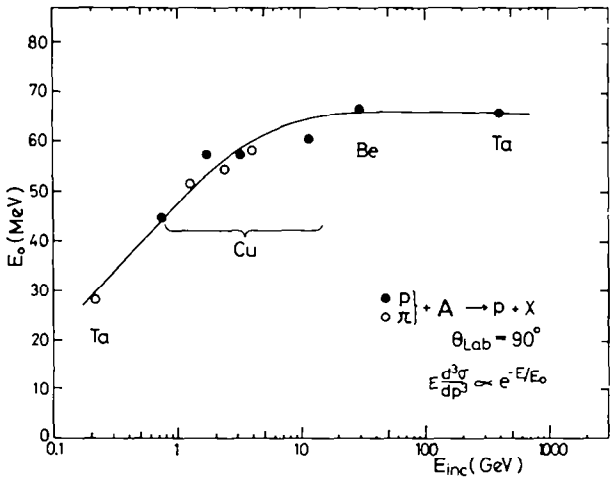

Fig. 12. The slope parameters E_0 as a function of incident projecile energy. Data points at 0.24, 12, 30 and 300 GeV are from refs. [15,12,16,17]), respectively.

mean kinetic energy per nucleon, since the mean kinetic energy is expressed as

$$\langle E\rangle = \iint E_{\mathrm{kin}} \frac{\mathrm{d}^2\sigma}{\mathrm{d}E\,\mathrm{d}\Omega}\,\mathrm{d}E\,\mathrm{d}\Omega \Big/ \iint \frac{\mathrm{d}^2\sigma}{\mathrm{d}E\,\mathrm{d}\Omega}\,\mathrm{d}E\,\mathrm{d}\Omega\,. \tag{8}$$

$\langle E\rangle$ is roughly equal to $\frac{3}{2}E_0$ when β_s is small.

As shown in fig. 12, the value of the E_0 parameter increases with incident projectile energy and saturates at the beam energy slightly below 10 GeV. It indicates the saturation of the target excitation or limitation of energy deposition in the target-rapidity region. The possible change of reaction mechanism around 5 to 10 GeV has previously been suggested by a number of experiments.

4.3. TWO-PROTON COINCIDENCE DATA

As described in the previous section, spectra of protons emitted in the highly inelastic process have indicated the formation of a single moving source. In this section, we deduce cross sections $\sigma_{\mathrm{h.i.}}$ for such highly inelastic processes and mean multiplicities $\langle m_{\mathrm{p}}\rangle$ of emitted protons from the two-proton coincidence data among the seven $\Delta E - E$ telescopes. The single $\mathrm{Y1}(\theta_j)$ and twofold coincidence $\mathrm{Y2}(\theta_j, \theta_k)$ counting rates of protons detected by the telescopes are given as

$$\mathrm{Y1}(\theta_j) = \sigma_{\mathrm{h.i.}}\langle m_{\mathrm{p}}\rangle IRN\Omega_j F_j\,, \tag{9}$$

$$\mathrm{Y2}(\theta_j, \theta_k) = \sigma_{\mathrm{h.i.}}\langle m_{\mathrm{p}}(m_{\mathrm{p}}-1)\rangle IRN\Omega_j\Omega_k F_j F_k \qquad (j \neq k)\,, \tag{10}$$

$$F_j = \int_{\Omega_j(\theta_j)} \mathrm{d}\Omega \int_{E_{j1}}^{E_{j2}} \mathrm{d}E\, f(\theta, E)\,, \tag{11}$$

where I and N are the beam intensity (particles/sec) and the target thickness (nuclei/cm^2). R is the fraction of protons or pions in the beam. The detection

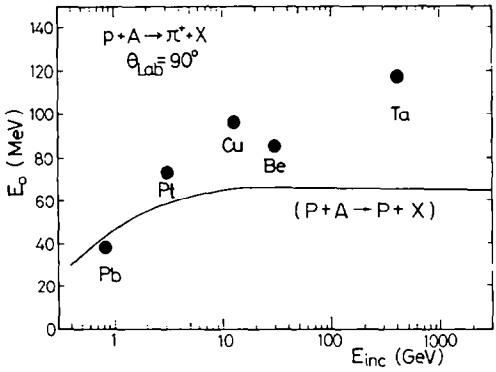

Fig. 13. The slope parameter E_0 for pions at $\theta_{\mathrm{lab}} = 90°$ versus incident projectile energy. The data points at 0.73, 2.9, 12, 30 and 400 GeV were taken from refs. [12,16 19]), respectively. The solid curve is the E_0 for emitted protons taken from fig. 12.

efficiency, energy cuts on proton spectra and the solid angle of each telescope are given by Ω_j, E_{j1}, E_{j2} and $\Omega_j(\theta_j)$, respectively. The single-moving-source model was used to calculate the normalized energy and angular distribution of protons $f(\theta, E)$. The Poisson distribution of m_p was assumed [20]) to use a relation $\langle m_p(m_p-1)\rangle = \langle m_p\rangle^2$. The parameters $\sigma_{h.i.}$ and $\langle m_p\rangle$ were determined by fitting all $14(=7\times 2)$ relations to the experimental data. The results are shown in table 7 and fig. 14.

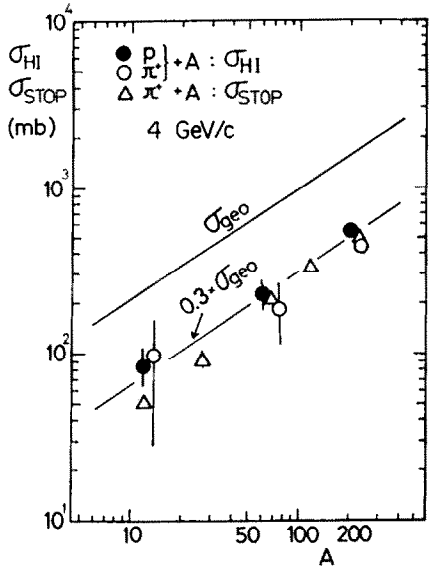

Fig. 14. Cross sections, $\sigma_{h.i.}$, for the formation of the moving source in a highly inelastic process. Data points shown by triangles are the "stopping" cross sections in fig. 11, determined from different experimental data (subsect. 4.4).

As shown in fig. 14, the cross sections for formation of the moving source deduced here are in good agreement with the "stopping" cross section deduced in subsect. 4.4 from totally different experimental data. The good agreement seems to indicate the correspondence between the moving-source-formation event and the "stopping" event defined as the event with multiparticle emission in the target region but no forward particle(s). Indeed, the protons emitted at large angles were suppressed considerably when a forward particle was emitted. The data shown by triangles in fig. 4 are proton spectra at 90° with a trigger condition requiring at least one particle in the forward counters ($\theta \leqslant 10°$). The data are only 10% of the inclusive 90° spectra (shown by squares), and those are mostly ascribed to events triggered by one of multiparticles emitted forward from the source.

Assuming that the incident particle stopped in the target nucleus and full energy and momentum transfer to the moving source took place, we made a crude estimate of a number of involved nucleons (or baryons) ν from the source velocity β_s:

$$\beta_s = p_{inc}/(E_{inc} + \nu M)\,, \tag{12}$$

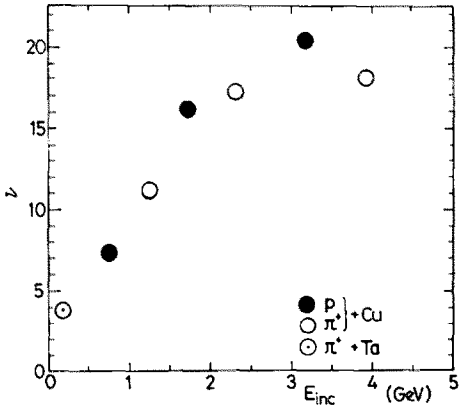

Fig. 15. The number of nucleons, ν, involved in the moving-source formation versus incident projectile energy. The point at 0.24 GeV is from ref. [15]).

where M is the nucleon mass. Values ν for a copper target are plotted as a function of incident energy in fig. 15. The value increases with incident energy and seems to saturate at around 3 GeV. The lowest-energy point in the figure was taken from ref. [15]). The ν-value in the π-nucleus reactions in the (3, 3) resonance region is compatible with the present result.

The target-mass dependences of ν for 4 GeV/c proton and pion reactions are shown by the circles in fig. 16. The number was given as

$$\nu = 5A^{1/3}. \tag{13}$$

The $A^{1/3}$ dependence is consistent with the linear-tube model for formation of the source. The diameter of the tube would then be about 6 fm.

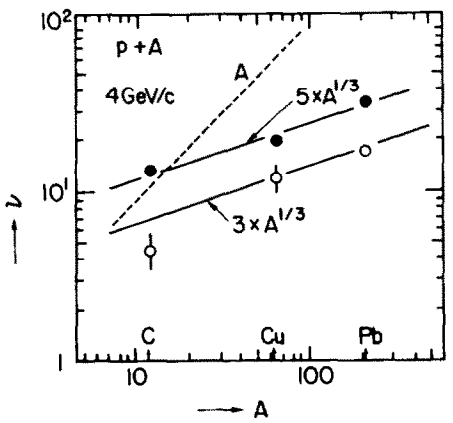

Fig. 16. Target-mass dependences of ν, the number of involved nucleons deduced from β_s (closed circles) and of $\langle n \rangle = (A/Z)\langle m_p \rangle$ (open circles), the mean multiplicity of emitted nucleons. The lines were drawn for comparison.

An alternative estimation is available from the mean proton multiplicities emitted from the source $\langle m_p \rangle$ determined above. The mean multiplicities of nucleons, deduced as

$$\nu' = \langle n \rangle = (A/Z)_{\text{target}} \langle m_p \rangle , \tag{14}$$

give the minimum number of ν. The numbers were smaller than those estimated from β_s as shown in fig. 16.

Considering the ambiguities in these analyses we may conclude that the number of nucleons involved in the source is

$$\nu = (3-5)\mathrm{A}^{1/3} . \tag{15}$$

Next, we tried to calculate energies carried away from the source by nucleons and pions, to check the energy balance in the "stopped" events. The results are plotted in fig. 17 for the copper target.

The energies carried away by nucleons were obtained simply by multiplying the average energy $\langle E \rangle$ calculated by the single-moving-source model by the mean nucleon multiplicity:

$$\langle E_p \rangle \langle n \rangle = \langle E_p \rangle (A/Z)_{\text{target}} \langle m_p \rangle . \tag{16}$$

They were about 45% of the incident energy.

The present experimental data were not sufficient to estimate the pion part, so that we had to make a crude estimate assuming that pions were emitted isotropically from the source with multiplicities $\langle m_\pi \rangle$ estimated from the (charged) pion-to-proton ratios $r = (N_{\pi^+} + N_{\pi^-})/N_p$ measured at 90° as the $\langle m_\pi \rangle = \frac{3}{2} r \langle m_p \rangle$. The average pion kinetic energy was estimated from the E_0 parameters of the pion spectra at 90° in

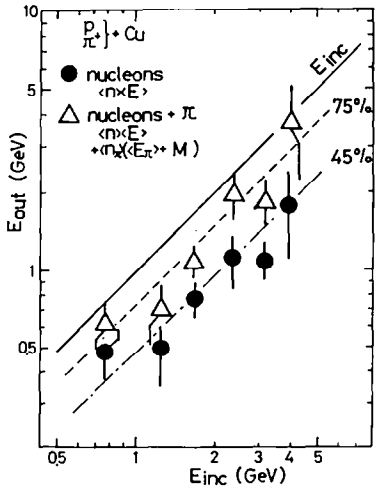

Fig. 17. Energies carried away by nucleons and pions.

fig. 13. in which data were compiled from other experiments. The energy taken out by pions is, then,

$$(\langle E_\pi \rangle + M_\pi)\langle m_\pi \rangle , \tag{17}$$

where M_π is the mass of pion.

Adding both pion and proton contributions, the estimates of the average energies emitted from the source amounted to about 75% of incident energy. The ambiguities in the estimates are so large that the significance of the remaining 25% is not obvious, but some parts of the incident energy must be dissipated for excitation of target fragments. Also, deuteron or composite particle emissions should not be negligible [13].

Hence it is reasonable to consider that the incident particle was stopped in a target nucleus, transferring its energy to excite the target and to form the moving source.

4.4 THE "STOPPING" PROCESS OF GeV PARTICLES

In the previous subsections, we have shown that the high-multiplicity events observed with the CyMWPC are the "stopped" events. In those events, the incident particle stops and deposits its energy in a target nucleus to form a localized moving source. In this section we shall discuss the "stopping" process.

For determination of the "stopping" cross section, σ_{stop}, the charged-particle multiplicity distributions, $F(m)$, measured with the CyMWPC were fitted with the formula

$$F(m) = A \exp(-Bm) + CP(\bar{m}, m) , \tag{18}$$

$$P(\bar{m}, m) = (\bar{m}^m / m!) \exp(-\bar{m}) , \tag{19}$$

where A, B, C, and $\bar{m}$ were free parameters. Then, the "stopping" cross sections were defined as

$$\int_0^\infty CP(\bar{m}, m)\, \mathrm{d}m = C = IRN\sigma_{\text{stop}} . \tag{20}$$

The beam intensity and fraction of protons or pions in the beam were given by I (beam-particles/sec) and R, and N was the target thickness in (nuclei/cm^2).

In this deduction of σ_{stop}, the efficiency of CyMWPC did not cause uncertainties, and statistical errors were sufficiently small. However, we have to allow systematic uncertainties of probably up to 30% due to ambiguities in this way of evaluating the cross sections. As shown in fig. 6b the multiplicity distribution with a trigger condition requiring no forward particle deviates from the Poisson distribution in the low-multiplicity part. This part amounts up to 25 to 30%, and may cause an underestimate of σ_{stop}. We ignored this part because most events in this part must be quasielastic scatterings.

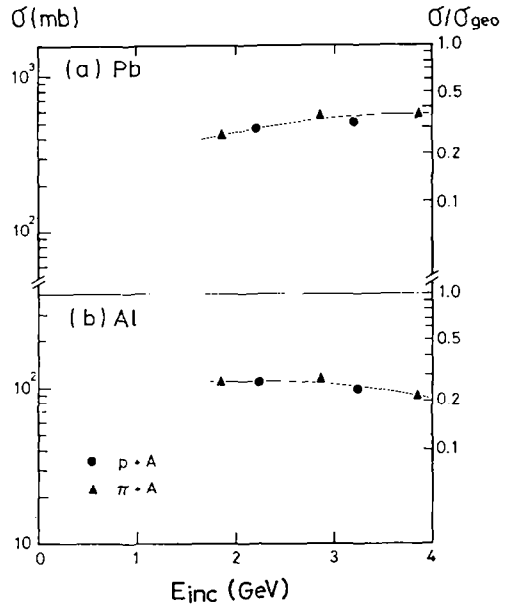

Fig. 18. "Stopping" cross sections versus incident projectile energy.

The "stopping" cross sections obtained are shown in fig. 11, which indicates that the "stopping" cross sections amounted to 30% of the geometrical cross sections, or the total reaction cross sections. The "stopping" cross sections are shown in fig. 18 as a function of incident energy. It was unexpected that the cross sections do not change up to 4 GeV even for a small nucleus such as aluminum.

It should be remembered that the "stopping" does not necessarily mean stopping of the projectile particle but stopping of its energy flow. The projectile energy has to be absorbed in the target nucleus. It is generally believed that nuclei would become transparent at higher energies and nuclear interactions would become less collective than in the low-energy region. This is not correct, at least up to the energy we studied. Below 2 GeV the mechanisms for energy dissipation of projectile in nuclear matter are multiple scatterings and the single-Δ formation. Above 2 GeV, however, many channels open, such as double-Δ formations and excitation of higher-mass resonances (excited baryons). The "stopping" power of nuclear matter must, therefore, increase with incident energy. Indeed, in fig. 18 a slight tendency of increasing cross section with incident energies is seen for the heavy nucleus Pb.

It is of great interest to know at what energy the "stopping" cross section starts decreasing. The present experiment did not provide any data to answer this question. However, the turning point in fig. 12 around 10 GeV, where the E_0 parameter starts to saturate, implies a change in the target excitation mode.

4.5. THREE COMPONENTS IN NUCLEON SPECTRA

The protons measured by the $\Delta E - E$ telescopes were limited in the energy range from 40 to 170 MeV. In this experiment, since thick targets had to be used to compensate for low beam intensities, the low-energy parts were not measurable, and the discussions in the previous subsections have focused mainly on the high-energy component from the local moving source.

In a previous experiment [12,13]), however, we observed a low-energy component in the proton spectra at 90° from the 12 GeV proton nucleus reactions as shown in fig. 8. The spectra in the figure were well reproduced by two components as

$$E\frac{\mathrm{d}^3\sigma}{\mathrm{d}p^3} = A_{\mathrm{I}} \exp(-E/E_0^{\mathrm{I}}) + A_{\mathrm{II}} \exp(-E/E_0^{\mathrm{II}}) . \tag{21}$$

The parameters E_0^{I} and E_0^{II} obtained by fitting the formula to the data are listed in table 8. They were $E_0^{\mathrm{I}} \simeq 60$ MeV and $E_0^{\mathrm{II}} = 6$–8 MeV, almost independent of the target nuclei. The first component with $E_0^{\mathrm{I}} \simeq 60$ MeV must correspond to the protons from the moving source as discussed above, while the second component with $E_0^{\mathrm{II}} = 6$–8 MeV seems to be the one which has been observed rather commonly in high-energy nuclear reactions. Those were often misassigned as evaporated particles.

TABLE 8

Parameters of two components in proton spectra emitted at 90° from 12 GeV protons on nuclei

Target	E_0^{II} (MeV)	E_0^{I} (MeV)	A^{II} (b/sr · (GeV/c)^2c)	A^{I} (b/sr · (GeV/c)^2c)
C		60.2 (6)		0.85 (1)
Al	7.43 (9)	56.6 (5)	12.5 (3)	2.21 (2)
Cu	6.59 (9)	55.9 (5)	59.1 (1.5)	7.01 (7)
Ag	7.74 (11)	57.8 (4)	72 (2)	10.3 (1)
Ta	8.09 (11)	59.4 (5)	123 (4)	14.9 (2)

In the present experiment, however, we observed a third component in the neutron spectra, the evaporated neutrons. The neutron spectrum in fig. 5 was reproduced as

$$E\frac{\mathrm{d}^3\sigma}{\mathrm{d}p^3} = \mathrm{A_I} \exp(-E/E_0^{\mathrm{I}}) + A_{\mathrm{II}} \exp(-E/E_0^{\mathrm{II}}) + A_{\mathrm{III}} \exp(-E/E_0^{\mathrm{III}}) , \tag{22}$$

and the parameters were $E_0^{\mathrm{I}} = 43$ MeV, $E_0^{\mathrm{II}} = 6$–8 MeV and $E_0^{\mathrm{III}} = 1.5$ MeV (table 9). The component with $E_0^{\mathrm{III}} = 1.5$ MeV must correspond to the evaporated

TABLE 9

Three components in neutron spectra emitted at 60° from Cu at 3 GeV/c

Reaction	E_0^{I}	E_0^{II} (MeV)	E_0^{III}	A^{I}	A^{II} (b/sr · (GeV/c)^2c)	A^{III}
p + Cu	43.2 (7)	7.92 (10)	1.60 (3)	9.0 (4)	260 (8)	13 200 (70)
π + Cu	42.8 (1.5)	5.98 (12)	1.26 (6)	14.6 (9)	678 (30)	28 500 (900)

Invariant cross sections were fitted with a function of $A^{\mathrm{I}}\exp(-E/E_0^{\mathrm{I}})+A^{\mathrm{II}}\exp(-E/E_0^{\mathrm{II}})+A^{\mathrm{III}}\exp(-E/E_0^{\mathrm{III}})$.

neutrons. This component is generally not easy to observe in proton spectra because of the Coulomb-barrier effect as well as absorption in the target.

The three components in the nucleon spectra seem to be emitted in three stages with different time scales which we may denote

(I) primary state, $E_0^{\mathrm{I}} = 30$–60 MeV,

(II) pre-equilibrium stage, $E_0^{\mathrm{II}} = 6$–8 MeV, and

(III) equilibrium stage (the evaporation), $E_0^{\mathrm{III}} = 1$–2 MeV.

The particle emission, particularly in stage I, must depend strongly on the impact parameter. In peripheral processes, high-momentum particle(s) are emitted in the forward direction in stage I instead of the multiparticles with $E_0^{\mathrm{I}} = 30$–60 MeV.

A difference in time scale between stages I and II was noted previously in our measurement and analysis of composite-particle productions from the 12 GeV protons on nuclei [13]). A result of the analysis is shown in fig. 10. In this analysis we were able to fit d, ^{3}He and ^{4}He data with the coalescence model, but when we calculated proton spectra from the composite-particle spectra we observed some excess protons in the low-energy region. We assumed this part to correspond to protons emitted in a slower time scale and which did not contribute to the coalescence process. Now is it obvious that those are the protons emitted in stage II.

Nucleon and nuclear fragment spectra with $E_0 = 6$–8 MeV or 6–8 MeV/nucleon have been reported in various cases, such as projectile and target fragmentation in high-energy heavy-ion reactions [21]), target fragmentation in proton–nucleus reactions [22]), and "direct" nucleons in pion-capture processes [23]). The pre-equilibrium nucleons in low-energy nuclear reactions [24]) would also be the same kind. These particles are considered to be emitted at the stage of "repairing" a "wounded" nucleus. After high-energy reactions, target (or projectile) nuclei would be left wounded, a part of their bodies being scraped off in the primary stage. From the analyses of momentum distributions of projectile fragments in high-energy heavy-ion reactions, Goldhaber [25]) has pointed out that the momentum distribution deduced from a simple Fermi motion with minimal correlation among nucleons corresponds to a temperature of about 9 MeV. It would be extremely interesting to study spatial correlations of this component for hunting nuclei with exotic shapes such as a doughnut shape, half-moon shape etc. [26]).

After emission of the pre-equilibrium particles, the nucleus would become a normal one and cool down by evaporating the residual energy.

5. Summary and remarks

5.1. SUMMARY

We have studied the highly inelastic processes in hadron–nucleus reactions at several GeV by measuring multiparticle emission in the target-rapidity region. Analyzing the present data, and partly using data from previous experiments, we obtained the following results:

(i) In measurements of the charged-particle multiplicity distribution and its correlation with forward particles, we observed events with no leading particle(s) in the forward direction but with multiparticles in the target region. Cross sections for such "stopped" events amounted to 30% of geometrical cross sections and were nearly constant over the incident projectile energy range from 1 to 4 GeV.

(ii) Inclusive proton spectra were well reproduced with a single-moving-source model which implies the formation of a slowly moving fire-ball-like object in the target region. The source velocity was $\beta_s = 0.1$–0.2, and the number of nucleons involved in the source was estimated to be $\nu = (3$–$5)A^{1/3}$.

(iii) Cross sections for formation of the moving source deduced from two-proton coincidence data were about 30% of the geometrical cross section, in good agreement with the "stopping" cross section, deduced using a different method.

(iv) The E_0 parameters of the proton spectra (given as $E\,\mathrm{d}^3\sigma/\mathrm{d}p^3 = A\exp(-E/E_0)$) increase with incident energy in the several GeV region but saturate at energies above 10 GeV.

(v) Three components were observed in nucleon spectra which would correspond to three stages: (I) primary, (II) pre-equilibrium and (III) equilibrium. Corresponding E_0 parameters of spectra were (I) 30–60 MeV, (II) 6–8 MeV and (III) 1–2 MeV.

Summarizing these results, we may draw the following picture for the highly inelastic process at several GeV:

When a hadron with an energy of several GeV hits a nucleus, it will be stopped and deposit its energy in the nucleus to form a fireball-like object moving with $\beta_s = 0.1$–0.2 in the target region with a probability of 0.3.

(I) Then, the fireball-like object will immediately decay, emitting nucleons (with $E_0 = 30$–70 MeV) and pions, leaving a wounded nucleus or nuclear fragments.

(II) The highly excited wounded nucleus (or fragments) emits nucleons (s) (with $E_0 = 6$–8 MeV) before the system reaches equlibrium.

(III) After equilibration, the nucleus will still be excited and cool down by evaporating additional nucleons (with $E_0 = 1$–2 MeV).

It is of interest to know whether the fireball-like object decays inside or outside the nucleus. The $A^{1/3}$ dependence of ν seems to indicate that the nucleons in a

tube-like formation zone must be involved to make the fireball at the end (outside the nucleus).

5.2. IMPLICATION FOR HEAVY-ION REACTIONS

The finding in the present work that the "stopping" power of nuclei increases with incident projectile energy in the several GeV region is very encouraging. The probability of producing a high-energy density must increase in high-energy heavy-ion reactions.

It was natural to believe that in nucleus-nucleus collisions the higher energy would not be suitable for observation of collective effects in the "nucleonic" matter. At the Bevalac, many survey experiments for possible nuclear collective effects were carried out at lower energies such as at 0.4 or 0.8 GeV/nucleon, for instance. However, also at higher energies, such as 5 to 10 GeV/nucleon, we may expect collective effects involving hadronic excitations.

The saturation of the E_0 parameters shown in fig. 12 appeared to be discouraging. However, as shown in fig. 13, the E_0 parameters for emitted pions are larger than those for protons. This might mean that a higher energy density was realized *before* the emission of protons. It is very interesting to compare the E_0 parameters for different secondary particles such as kaons, photons or lepton pairs as well as for pions and protons [27]).

The picture drawn in the summary for the hadron–nucleus reaction implies that also in heavy-ion reactions there must be rather well-defined sources (slow-moving fireballs) in the fragmentation regions, in addition to the central fireball. Since the (central) fireball model was proposed by Westfall *et al.* [28]), the model had to be refined to compare with experimental data, and several models such as the firestreak model [29]), the two-fireball model [30]) etc. have been proposed. Those models had emphases on more particle emissions from the near-fragmentation regions than the original fireball model. Recently, an experimental indication for such sources in the fragmentation regions were reported by Manko and Nagamiya [31]).

It is certain that the central fireball should have a higher temperature than those in the fragmentation regions, but it is not certain which fireball would be more suitable to study possible nuclear collective phenomena at high energy.

We wish to thank Professors T. Nishikawa and S. Ozaki, and staff members of KEK for support during the present experiments. We are much obliged to Professors T. Fujita, S. Nagamiya, M. Sano, I. Tanihata, K. Yazaki, Y. Yamaguchi and T. Yukawa for their advice, discussions and criticism. The continuous interest and encouragement by Professors A. Kusumegi and T. Yamazaki are gratefully acknowledged. This work was partly supported by the Grant-in-Aid for Scientific Research by the Ministry of Education, Culture and Science, Japan.

References

1) K. Nakai, T.-A. Shibata, H. En'yo, S. Sasaki, M. Sekimoto, I. Arai, K. Nakayama, K. Ichimaru, H. Nakamura-Yokota and R. Chiba, Phys. Lett. **121B** (1983) 373
2) T.-A. Shibata, thesis, University of Tokyo (1982) UTPN-179
3) A.B. Migdal, Rev. Mod. Phys. **50** (1978) 107;
G.E. Brown and W. Weise, Phys. Reports **27** (1976) 1;
G. Baym, in Proc. 1977 Les Houches Summer School, ed. R. Balian and G. Ripka (North-Holland, Amsterdam, 1978) 745;
M. Jacob and J. Tran Thanh Van, Phys. Reports **88C** (1982) 321
4) S. Nagamiya and M. Gyulassy, High-energy nuclear collisions in Advance in nuclear physics **13** (Plenum, NY, 1983) 199 and references theirein
5) A.S. Goldhaber, in High-energy nuclear interactions and property of dense nuclear matter (Proc. Hakone Seminar, 1980) ed. K. Nakai and A.S. Goldhaber
6) J.-I. Fujita, Butsuri **30** (1975) 344;
K. Nakai, J. Chiba, I. Tanihata, M. Sasao, H. Bowman, S. Nagamiya and J.O. Rasmussen, Phys. Rev. **C20** (1979) 2210
7) KEK Experiment E90, unpublished
8) H. En'yo, M. Sekimoto and K. Nakai, Nucl. Instr. **196** (1982) 29
9) F.T. Kuchinir and F.J. Lynch, Trans. IEEE **NS-15** (1968) 107
10) M. Drosg, Nuc. Instr. **105** (1972) 573
11) R.S. Hayano and J. Chiba, CAMAC control system for PDP-11 and VAX-11 (CCS-11) (in Japanese) KEK internal report 82-3 (1982)
12) T.-A. Shibata, T. Kobayashi, T. Numao, J. Chiba, K. Nakai, T. Yamazaki, O. Hashimoto, H. Hamagaki, M. Taino, A. Yamamoto, S. Kurokawa and H. Hirabayashi, Nucl. Instr. **179** (1981) 67
13) K. Nakai, O. Terasaki, T.-A. Shibata, H. En'yo and I. Arai, Phys. Rev. **C25** (1982) 1992
14) Meng Ta-Chung and E. Moeller, Phys. Rev. Lett **41** (1978) 1352;
I.G. Bogatskaya, C.B. Chiu, M.I. Gorenstein and G.M. Zinovjev, Phys. Rev. **C22** (1980) 209
15) R.D. McKeown, S.J. Sanders, J.P. Schiffer, H.E. Jackson, M. Paul, J.R. Speckt, E.J. Stepehenson, P.R. Redwine and R.E. Segel, Phys. Rev. Lett. **44** (1980) 1033
16) V.L. Fitch, S.L. Meyer and P.A. Piroué, Phys. Rev. **126** (1962) 1849
17. Y.D. Bayukov, V.I. Efremenko, S. Frankel, W. Frati, M. Gazzaly, G.A. Leksin, N.A. Nikiforov, C.F. Perdrisat, V.I. Tchistilin and Y.M. Zaitsev, Phys. Rev. Lett. **85B** (1979) 315
18) D.R.F. Cochran, P.N. Dean, P.A.M. Gram, E.A. Knapp, E.R. Martin, D.E. Nagle, R.B. Perkins, W.J. Shlaer, H.A. Thiessen and E.D. Therlot, Phys. Rev. **C6** (1972) 3085
19) P.A. Piroué and A.J.S. Smith, Phys. Rev. **148** (1966) 1315
20) A. Sandoval, R. Stock, H.E. Stelzer, R.E. Rendordt, J.W. Harris, J.P. Brannigan, J.V. Geaga, L.J. Rosenberg, L.S. Schroeder and K. Wolf, Phys. Rev. Lett. **45** (1980) 874
21) H.H. Heckman, H.J. Crawford, D.E. Greiner, P.J. Lindstrom and L.W. Wilson, Phys. Rev. **C17** (1978) 1651
22) A.M. Poskanzer, G.W. Butler and E.K. Hyde, Phys. Rev. **C3** (1971) 882
23) R. Hartman, H.P. Isaak, R. Engfer, E.A. Hermes, H.S. Pruys, W. Dey, H. Pfeiffer, V. Sennhauser, H.K. Walter and J. Morgenstern, Nucl. Phys. **A308** (1978) 345
24) H. Ejiri, T. Itahashi, Y. Nagai, T. Shibata, S. Nakayama, T. Kishimoto, K. Maeda, H. Sakai and M. Hoshi, Nucl. Phys. **A305** (1978) 167, and references therein
25) A.S. Goldhaber, Phys. Lett. **53B** (1972) 306
26) H. Morinaga, J. de Phys. Suppl. 33 (1972) C5-103;
Y. Yamaguchi, Progr. Theor. Phys. **67** (1982) 1810
27) S. Nagamiya, Phys. Rev. Lett. **49** (1982) 1383
28) G.D. Westfall, J. Gosset, P.J. Johansen, A.M. Poskanzer, W.G. Meyer, H.H. Gutbrod, A. Sandoval and R. Stock, Phys. Rev. Lett. **37** (1976) 1202
29) W.D. Meyer, Nucl. Phys. **A296** (1978) 177
30) Y. Kitazoe, M. Sano and K. Yamamoto, J. Phys. Soc. Japan Suppl. 44 (1978) 386;
S. Das Gupta, Phys. Rev. Lett. **41** (1978) 1450
31) V.I. Manko and S. Nagamiya, Nucl. Phys. **A384** (1982) 475